

1 **Measurement report: Sources, sinks and lifetime of NO_x in a sub-**
2 **urban temperate forest at night**
3

4 Simone T. Andersen¹, Max R. McGillen², Chaoyang Xue², Tobias Seubert¹, Patrick Dewald¹,
5 Gunther N. T. E. Türk¹, Jan Schuladen¹, Cyrielle Denjean³, Jean-Claude Etienne³, Olivier
6 Garrouste³, Marina Jamar⁴, Sergio Harb⁵, Manuela Cirtog⁵, Vincent Michoud⁶, Mathieu
7 Cazaunau⁵, Antonin Bergé⁵, Christopher Cantrell⁵, Sebastien Dusanter⁴, Bénédicte Picquet-
8 Varrault⁵, Alexandre Kukui⁷, Abdelwahid Mellouki^{2,8}, Lucy J. Carpenter⁹, Jos Lelieveld¹, John N.
9 Crowley¹

10 ¹Atmospheric Chemistry Department, Max-Planck-Institute for Chemistry, 55128-Mainz,
11 Germany

12 ²Institut de Combustion, Aérothermique, Réactivité Environnement (ICARE), CNRS, 1C Avenue
13 de la Recherche Scientifique, CEDEX 2, 45071 Orléans, France

14 ³CNRM, Université de Toulouse, Météo-France, CNRS, Toulouse, France

15 ⁴IMT Nord Europe, Institut Mines-Télécom, Université de Lille, Center for Energy and
16 Environment, 59000 Lille, France

17 ⁵Univ Paris Est Creteil and Université de Paris Cité, CNRS, LISA, F-94010 Créteil, France

18 ⁶Université Paris Cité and Univ Paris Est Creteil, CNRS, LISA, F-75013 Paris, France

19 ⁷Laboratoire de Physique et Chimie de l'Environnement et de l'Espace (LPC2E), CNRS Orléans,
20 France

21 ⁸University Mohammed VI Polytechnic (UM6P), Lot 660, Hay Moulay Rachid Ben Guerir, 43150,
22 Morocco

23 ⁹Wolfson Atmospheric Chemistry Laboratory, Department of Chemistry, University of York,
24 York, UK

25 *Correspondence to:* Simone T. Andersen (simone.andersen@mpic.de) and John N. Crowley
26 (john.crowley@mpic.de)

27

28 **1 Abstract**

29 Through observations of NO, NO₂, NO_Y and O₃ in the Rambouillet forest near Paris, France, (as
30 part of the ACROSS campaign, 2022) we have gained insight into nighttime processes controlling
31 NO_X in an anthropogenically impacted forest environment. O₃ mixing ratios displayed a strong
32 diel profile at the site, which was driven by a variable but generally rapid deposition to soil and
33 foliar surfaces. The O₃ diel profile was strongly influenced by relative humidity, which impacted
34 the surface resistance to uptake, and temperature inversion, which influenced the rate of
35 entrainment of O₃ from above the canopy. Only when the O₃ mixing ratio was sufficiently low
36 (and thus the NO lifetime sufficiently long), were sustained NO peaks observed above the
37 instrumental detection limit, enabling derivation of average NO emission rates from the soil of
38 ~1.4 ppbv h⁻¹. Observations of the lack of increase in NO₂ at night, despite a significant production
39 rate from the reaction of NO with O₃, enabled an effective lifetime of NO₂ of ~0.5-3 h to be
40 derived. As the loss of NO₂ was not compensated by the formation of gas- or particle-phase
41 reactive nitrogen species it was presumably driven by deposition to soil and foliar surfaces, or any
42 products formed were themselves short-lived with respect to deposition. By comparison, the
43 daytime lifetime of NO₂ with respect to loss by reaction with OH is about 1 day. We conclude that
44 the nighttime deposition of NO₂ is a major sink of boundary layer NO_X in this temperate forest
45 environment.

46

47 **2 Introduction**

48 Nitrogen oxides (NO_X = NO + NO₂) are pollutant trace gases, which play a key role in the
49 atmosphere by producing or destroying tropospheric ozone (O₃), which can cause respiratory
50 illness (Ciencewicki and Jaspers, 2007) and damage to plants (Emberson et al., 2018). Photolysis
51 of nitrogen dioxide (NO₂) (R1) is the primary source of tropospheric ozone (O₃), and the nitric
52 oxide (NO) product is oxidized back to NO₂ either by O₃ (R2) or by organic peroxy radicals (RO₂,
53 under formation of alkoxy radicals (RO)) or hydroperoxyl radicals (HO₂) (R3, R4) (Lightfoot et
54 al., 1992). The latter results in formation of the hydroxyl radical (OH) radical, and R3 and R4 thus
55 represent routes to recycle the most important atmospheric radical initiator of oxidation (Hens et
56 al., 2014). It is, therefore, essential to understand the sources and sinks of NO_X in the atmosphere.



61 The dominant global sources of NO_X are anthropogenic in the form of combustion of fossil fuels
62 and to a lesser degree biomass burning and agricultural soils. The natural sources, which include
63 lightning (Schumann and Huntrieser, 2007), wildfires (Val Martin et al., 2008), and unperturbed
64 soil emissions from microbial activities (Davidson and Kinglerlee, 1997), are important in regions
65 remote from anthropogenic sources. NO₂ and NO both react with peroxy radicals in the atmosphere

66 to produce organic nitrates (R5-R6), including peroxy nitrates (RO_2NO_2) and alkyl nitrates
 67 (RONO_2), which are important precursors for the formation of secondary organic aerosols (SOA)
 68 (Hallquist et al., 2009; Kanakidou et al., 2005; Kiendler-Scharr et al., 2016). NO_2 also reacts with
 69 OH radicals, O_3 and nitrate radicals (NO_3) to form nitric acid (HNO_3) (R7), NO_3 radicals (R8), and
 70 dinitrogen pentoxide (N_2O_5) (R9), respectively. N_2O_5 is in thermal equilibrium with NO_2 and NO_3
 71 and can interact with aqueous aerosol or moist surfaces to form HNO_3 (R10) (Kane et al., 2001)
 72 or nitryl chloride (ClNO_2) (Phillips et al., 2013; Phillips et al., 2012). Organic nitrates, SOA, and
 73 HNO_3 are all removed from the boundary layer through dry and wet deposition which thereby
 74 removes NO_x from the atmosphere.



81 In the planetary boundary layer, NO_2 is also lost through dry deposition to surfaces such as soil
 82 and leaves. Deposition takes places both at nighttime and daytime, but is expected to be more
 83 efficient during daytime due to increased mixing through turbulence. When NO_2 deposits onto
 84 humid surfaces, it can lead to the production of nitrous acid (HONO), which can be released to the
 85 atmosphere (Meusel et al., 2016; Elshorbany et al., 2012). NO_2 uptake on leaves takes place
 86 through stomatal and non-stomatal processes, which have been reported to depend on multiple
 87 factors such as stomata aperture and relative humidity. Stomatal uptake primarily occurs at
 88 daytime when the stomata are open, leading to increased NO_2 loss compared to nighttime, when
 89 the stomata are not fully open (Delaria et al., 2020; Delaria et al., 2018; Chaparro-Suarez et al.,
 90 2011). Non-stomatal uptake occurs through the cuticles, though the importance of cuticular uptake
 91 has been reported to be small compared to the stomatal uptake (Delaria and Cohen, 2020; Delaria
 92 et al., 2020). NO_2 uptake to leaves is reported to be enhanced in the presence of water films, which
 93 may exist when the relative humidity is $>70\%$ (Thoene et al., 1996; Weber and Rennenberg, 1996;
 94 Burkhardt and Eiden, 1994). There is, however, no consensus on this process, as other studies have
 95 not observed this effect (Gessler et al., 2000). Most recent work shows that the interactions with
 96 foliar surfaces is uni-directional, i.e. emissions are negligible (Delaria et al., 2020).

97 At nighttime, NO_2 photolysis ceases and as a consequence, in the absence of combustion sources,
 98 the main sources of NO are emissions from soils (Jaeglé et al., 2005). Since NO is oxidised
 99 efficiently by O_3 at night, its concentration will be highest at the surface and will decrease with
 100 altitude. The vertical profile of O_3 is the opposite owing to its physical loss due to deposition near
 101 the surface and through chemical reaction with NO and/or alkenes combined with entrainment
 102 from the nocturnal residual layer. As NO_2 is produced from the reaction between NO and O_3 , its

103 vertical gradient is expected to be weaker than those of NO and O₃ (Geyer and Stutz, 2004; Stutz
104 et al., 2004).

105 In this study we use measurements from the ACROSS (Atmospheric ChemistRy Of the Suburban
106 foreSt) campaign to investigate the nighttime sources and sinks of NO_x in a temperate forest. O₃
107 measurements are used to explain the observed NO features and measurements of NO₂ and total
108 gas-phase nitrogen species (NO_y) and particulate nitrate are used to investigate the lifetime and
109 fate of NO_x in the forest environment.

110

111 **3 The ACROSS Campaign**

112 The ACROSS campaign (13th of June 2022 to 25th of July 2022) was conducted in multiple
113 locations in and around Paris, France (Cantrell and Michoud, 2022). Here we present
114 measurements from the Rambouillet forest supersite located approximately 50 km southwest of
115 Paris (48.687, 1.704). The forest consists of approximately 70% oak, 20% pine, and small
116 contributions from beech and chestnut. The top of the forest canopy around the supersite was
117 around 20-25 m. Several instrumented containers were placed in a clearing (~697 m²) together
118 with a 41 m measurement tower. Most of the instruments used in this study were located in two
119 different containers (MPIC and Orléans). The sampling inlets of the two containers were
120 approximately 17 m apart and the tower was approximately 9 m from the MPIC container and 16
121 m from the Orléans container. The soil measurements were carried out at the bottom of the tower,
122 approximately 13 m from the MPIC container and approximately 17 m from the Orleans container.
123 All the instruments used in this study are described briefly below.

124

125 **3.1 Measurements**

126 **3.1.1 Ground**

127 NO₂ was measured using two different cavity ringdown spectroscopy (CRDS) instruments with
128 co-located inlets sampling from a high-volume-flow stainless steel tube (10 m³ min⁻¹; 15 cm
129 diameter, 0.2 s residence time) taking air from a height of 5.4 m above ground. One of the
130 instruments (5CH-CRDS) consists of 3 cavities operated at 408 nm to measure NO₂ and, via their
131 thermal dissociation to NO₂, total peroxy nitrates (Σ PNs, 448 K) and total alkyl nitrates (Σ ANs,
132 648 K). Two additional cavities, operated at 662 nm, measured NO₃ and (via thermal dissociation
133 to NO₃, 373 K) N₂O₅ (Sobanski et al., 2016). During this campaign, the NO₂ cavity had a limit of
134 detection (LOD) of 9.7 pptv for 1 min averaging (3 σ). The second instrument (k-NO3) primarily
135 measures the NO₃ reactivity, but also has a cavity operated at 405 nm for the measurement of NO₂
136 (Liebmann et al., 2018).

137 Another CRDS instrument was used to measure NO_x, NO_y, and particulate nitrate (pNO₃) from
138 co-located inlets near the high-volume-flow stainless steel tube. NO_x was measured by adding O₃
139 to the ambient sample, thereby oxidizing NO to NO₂, which was measured with CRDS at 405 nm
140 (Friedrich et al., 2020). A judicious choice of O₃ and reaction time ensured that minimal (>1%) of
141 NO₂ was oxidized to NO₃. At times with low (or zero) NO, NO_x concentrations were in close

142 agreement with both NO₂ measurements. NO_Y was measured by passing ambient air through a
143 quartz inlet at ~ 900 K which quantitatively converts reactive nitrogen trace-gases to NO or NO₂.
144 Exceptions are N₂O, HCN and NH₃, which are not detected. In this location, NO_Y is expected to
145 consist mainly of NO_X + NO₃ + N₂O₅ + HNO₃ + PNs + ANs + HONO + ClNO₂ + particulate
146 nitrates (pNO₃).

147 Particulate nitrates (both organic and inorganic) were separately measured (as NO_Y) after denuding
148 gas-phase reactive nitrogen species (Friedrich et al., 2020). To achieve this, problems involving
149 the ineffective trapping of gas-phase NO_X by the denuder was eliminated, as will be described in
150 a forthcoming technical paper.

151 O₃ was measured from the high-volume-flow stainless-steel tube with a commercial instrument
152 (2B Technologies model 205) using UV absorption at 254 nm. The LOD is 2 ppbv for 10 s
153 averaging time.

154 A spectral radiometer (metcon GmbH) was installed near the co-located inlets on top of the MPIC
155 container to measure actinic fluxes, which were used to calculate photolysis frequencies as
156 described elsewhere (Meusel et al., 2016).

157 NO was measured from the Orléans container using a commercial chemiluminescence instrument
158 (Ecophysics CLD 780 TR, henceforth CLD) with an LOD of 10 pptv for 1 min averaging time.
159 The sampling height for NO measurements was about 0.6 and 3.2 m above the container top and
160 the ground surface, respectively. The NO measurements required correction due to a change in the
161 CLD sensitivity during the campaign caused by an interruption in the instrument's oxygen supply.
162 The corrections and the corrective procedure are described in the SI.

163 HONO was measured by a commercial long-path absorption photometer (LOPAP-03, QUMA
164 GmbH, Germany) with a sampling height of 2.0 m above the ground level. Details about the
165 LOPAP instrument can be found elsewhere (Heland et al., 2001; Kleffmann et al., 2006). During
166 the campaign, the LOPAP was calibrated by diluted nitrite when changing any supporting
167 solutions. Zero calibration by measuring synthetic air was conducted 2-3 times per day. The
168 detection limit is < 5 pptv.

169 The sum of peroxy radicals, XO₂=HO₂+RO₂, was measured by their conversion to H₂SO₄ in
170 presence of NO and SO₂ and detection of the generated H₂SO₄ using NO₃⁻ CIMS (Kukui et al.,
171 2008). The calibration coefficient is determined using N₂O actinometry and OH/RO₂ generation
172 in a turbulent flow reactor by photolysis of N₂O or H₂O at 184.9 nm. The calibration of HO₂,
173 CH₃O₂ and other RO₂ is performed by adding into the calibration reactor CO, CH₄ (or other RO₂
174 precursors) converting OH to RO₂. The overall estimated calibration accuracy (2σ) for XO₂ is
175 about 30%, although the uncertainty of the XO₂ measurements is typically higher due to
176 uncertainty in ambient air XO₂ composition. The lower limit of detection for XO₂ radicals at S/N=3
177 and a 4 minute integration time is 2×10⁶ molecule cm⁻³.

178 Time series of the most relevant measurements can be found in Figure S1-2. Due to missing total
179 NO_X and NO_Y measurements prior to June 25th and NO after July 18th, the data analysis is focused
180 on the time period in between these dates.

181

182 **3.1.2 Tower**

183 Measurements at 41 m were conducted with instruments located on the tower as well as through a
184 manifold with an inlet at the top of the tower. The manifold was built from glass tubing (4.9 cm
185 inner diameter, Borodrain) with a residence time in the manifold of 2.1 s. NO₂ was measured using
186 a cavity attenuated phase shift (CAPS) instrument on the tower with an LOD of 40 pptv, which
187 was zeroed every 1-2 hours. NO and O₃ were both measured from the manifold using a
188 chemiluminescence instrument with a LOD of 30 pptv and a HORIBA (APOA370) with an LOD
189 of 2.5 ppbv, respectively. The NO measurements were corrected for losses due to the reaction of
190 NO with O₃ in the manifold and the sampling line (total 5.5 s), with corrections ranging from 1-
191 28%. Time series of all three measurements are plotted in Figure S3.

192

193 **3.1.3 Meteorology and Soil**

194 Ambient temperature was measured at four different heights on the tower; 5 m, 13 m, 21 m, and
195 41 m using temperature sensors from Atexis (PT1000) and Thermoest (PT100). Relative humidity
196 was measured at 5 m using a Vaisala humidity sensor (HMP45A). Soil temperature and moisture
197 were measured at 5 cm, 10 cm, and 30 cm below the surface using probes from Thermoest (PT100)
198 and Delta T (Thetaprobe ML2X), respectively. Wind speed and direction were measured at 41 m
199 using a wind monitor from Young Company. Time series of all the meteorological and soil
200 measurements are shown in Figure S4-5.

201

202 **3.2 HYSPLIT**

203 To identify different air masses, 48-hour back trajectories were simulated every hour at a
204 terminating height of 40 m using the Hybrid Single-Particle Lagrangian Integrated Trajectory
205 model (HYSPLIT, version 4, 2019) (Draxler and Rolph, 2011). The back-trajectories were
206 modelled using meteorological data from the Global Data Assimilation System (GDAS) at a
207 resolution of 1 degree. This led to the separation of the data into two periods, 25th of June to 2nd of
208 July and 3rd of July to 18th of July, which are plotted in Figure 1. The first phase is dominated by
209 clean air from over the Atlantic Ocean (henceforth called “Atlantic”). Back trajectories indicated
210 that the vast majority of air masses were transported within the boundary layer prior to reaching
211 the site and thus may have reasonably fresh “marine influence”. The second phase is dominated
212 by air that has passed over urban locations including Paris, Brussels and the Ruhr area within the
213 last 48 hours (henceforth called “Continental”).

214

215 **4 Results and Discussion**

216 Two 24-hour periods of temperature (at 4 different heights), NO, O₃, relative humidity (RH), NO₂,
217 and NO₂ photolysis rate constant (JNO₂) are plotted in Figure 2. The left panels show 24 hours
218 with Atlantic air and the right panels 24 hours with continental air. Immediately apparent in these
219 datasets (and in Fig S1) is the large diel cycle in O₃ mixing ratios, with net daytime production

220 resulting in mid-afternoon mixing ratios between ~30 and 90 ppbv. In contrast, very low O₃ mixing
221 ratios (often approaching zero) were observed at nighttime.

222 In the lowermost panels (JNO₂ measurements), the nighttime is shown in dark grey and the two
223 light grey areas show the time before sunset (about 5 hours) and after sunrise (about 4.5 hours)
224 when very little direct sunlight reaches the ground of the site due to shading by the trees. This
225 leaves about 6.5 hours centred around midday when direct sunlight reaches the ground. The
226 shading results in radiative cooling of the ground in the late afternoon and associated temperature
227 inversions begin to form prior to sunset as can be observed in the right panels of Figure 2 and in
228 more detail in Figure S6. The temperature inversions begin approximately at the same time as the
229 ground temperature at 5 cm below the surface starts to decrease (see Figure S6). These conditions
230 of insolation were relatively consistent throughout the campaign.

231 Clear temperature inversions were observed for both nights shown in Figure 2, the beginning and
232 end of which are indicated by dashed lines. Vertical mixing can be reduced significantly during a
233 temperature inversion, which is apparent from the O₃ and RH measurements in the right-hand
234 panel. In both examples, O₃ decreases at the ground level (5.4 m) at the beginning of the
235 temperature inversion and increases as the inversion breaks down in the morning. This behaviour
236 is understood in terms of O₃ loss to soil surfaces and through stomatal and non-stomatal uptake on
237 leaves (Zhou et al., 2017; Rannik et al., 2012; Altimir et al., 2006; Ganzeveld and Lelieveld, 1995)
238 as well as through chemical reactions with e.g. NO, NO₂ and unsaturated (biogenic) organics
239 (Kurpius and Goldstein, 2003). Reduced vertical mixing means that during the inversion, O₃ is
240 only slowly replenished by downward mixing of air masses above the canopy where higher O₃
241 levels are observed. In contrast, the RH behaves in the opposite sense as the air above the inversion
242 is drier than close to the ground, where evapotranspiration contributes to enhanced water vapour
243 concentrations.

244 If the only source of NO was the photolysis of NO₂, NO mixing ratios would be expected to follow
245 the NO₂ photolysis rate during the day and tend to zero at night as NO is oxidized on a time scale
246 of minutes (for O₃ > 10 ppb) to NO₂ by O₃. This was not always the case during ACROSS. A
247 pronounced NO peak (up to ~2 ppbv) was observed at ground level between 00:00 and 06:00 UTC
248 (02:00 and 08:00 local time) during the phase dominated by Atlantic air, shown in Figure 2, which
249 is absent in the phase dominated by continental air. The peak occurs prior to sunrise and is only
250 observed by the ground-level measurements suggesting a non-photolytic source of NO close to the
251 ground, which is discussed further below. Very low (0-5 ppbv) O₃ mixing ratios coincide with the
252 sustained nighttime NO peak observed, which is never reached in the example from the continental
253 phase, although in both cases clear temperature inversions were seen. Additional examples of
254 sustained NO peaks (i.e. lasting several hours at level between 1 and 2 ppbv) at night during the
255 first phase are shown in Figure S7. Examples of additional nights with temperature inversions
256 during phase 2, where NO mixing ratios remained close to zero, are shown in Figure S8.

257

258 4.1 Nighttime Ozone Loss

259 For each night between June 17th and July 22nd the net O₃ loss rate constant, $k_L(\text{O}_3)$ was derived
260 by fitting exponential expressions to the data for periods of 4.5 to 8 hours. $k_L(\text{O}_3)$ was highly
261 variable, with values between $1.8 \times 10^{-5} \text{ s}^{-1}$ and $3.0 \times 10^{-4} \text{ s}^{-1}$, depending on the strength of the
262 temperature inversion and the relative humidity (see discussion below). These values of $k_L(\text{O}_3)$
263 correspond to lifetimes of 1-15 hours for O₃ at nighttime. Chemical losses of O₃ occur through
264 reactions with NO, NO₂, and unsaturated BVOCs (Zhou et al., 2017). Rate coefficients of reactions
265 of O₃ with NO ($1.9 \times 10^{-14} \text{ cm}^3 \text{ molecule}^{-1} \text{ s}^{-1}$ at 298 K), NO₂ ($3.5 \times 10^{-17} \text{ cm}^3 \text{ molecule}^{-1} \text{ s}^{-1}$ at 298
266 K), limonene (a reactive terpene, $2.2 \times 10^{-16} \text{ cm}^3 \text{ molecule}^{-1} \text{ s}^{-1}$ at 298 K), β -caryophyllene
267 (sesquiterpene, $1.2 \times 10^{-14} \text{ cm}^3 \text{ molecule}^{-1} \text{ s}^{-1}$ at 298 K) are low such that mixing ratios in excess
268 of 1 ppbv for NO and β -caryophyllene would be required to explain the O₃ loss rate constant
269 (IUPAC, 2024). Required mixing ratios of terpenes or NO₂ would be even larger (60-300 ppbv).
270 As such high mixing ratios of NO and NO₂ were not observed continuously and such levels of
271 BVOC are unlikely, we assume that chemical losses of O₃ are insignificant compared to deposition
272 as previously observed (Zhou et al., 2017). Ignoring entrainment from other heights, we can then
273 equate $k_L(\text{O}_3)$ to $(2V_d/h)$, where V_d is the deposition velocity and h is the boundary layer height;
274 the factor 2 is used to account for a positive vertical gradient (Shepson et al., 1992). Using a
275 boundary layer height of 20 m (arbitrarily set equal to the top of the canopy) gives net deposition
276 velocities varying between 0.018 and 0.3 cm s⁻¹. These values for V_d are in broad agreement with
277 other studies in temperate forests, where deposition velocities for O₃ at nighttime have been
278 reported to be around 0.07-0.3 cm s⁻¹ (Padro, 1996, 1993; Finkelstein et al., 2000; Wu et al., 2016).

279 In Figure 3 the O₃ production rate ($J\text{NO}_2 \times [\text{NO}_2]$), RH, temperature at 4 different heights and O₃
280 mixing ratio have been plotted for two nights with high average RH to illustrate the impact of
281 temperature inversions on the net O₃ loss-rate constants. The production rate of O₃ is used to
282 identify periods in which production is negligible. In the left panel a night without a temperature
283 inversion is plotted, where the average RH for the period used to fit the exponential decay is $93 \pm$
284 3% . These conditions resulted in a net O₃ loss-rate constant of $6.0 \times 10^{-5} \text{ s}^{-1}$. In contrast, the night
285 depicted in the right panel has the same average RH ($92 \pm 3 \%$) and a very clear temperature
286 inversion, which gives a net O₃ loss-rate constant of $3.0 \times 10^{-4} \text{ s}^{-1}$. This gives a factor of 5 between
287 these two net O₃ loss-rate constants depending on whether a temperature inversion is observed or
288 not. This can be understood in terms of the O₃ being replenished from above when there is no (or
289 a weak) inversion, which is not the case when there is an inversion. Bearing this in mind, the use
290 of $k_L(\text{O}_3)$ (a *net* O₃ loss constant) must result in a lower limit to V_d unless strong temperature
291 inversions (preventing O₃ entrainment from above) are present. The O₃ loss rate will also be
292 enhanced under conditions of strong inversion if trace-gases that are reactive towards O₃ are
293 released into a very shallow boundary layer. However, as indicated above, chemical losses are not
294 expected to compete with physical losses.

295 To investigate the impact of RH on the net O₃ loss-rate constants, two nights with temperature
296 inversions are plotted in Figure S9; one with high RH ($92 \pm 3 \%$) and one with a lower RH ($63 \pm$
297 6%). Here we see a large decrease in $k_L(\text{O}_3)$ from $3.0 \times 10^{-4} \text{ s}^{-1}$ to $4.5 \times 10^{-5} \text{ s}^{-1}$, when going from
298 high to lower RH. The individually determined O₃ loss-rate constants are plotted as a function of
299 RH in Figure 4 and coloured depending on whether a temperature inversion is observed or not

300 during the time period which was used for the exponential decay fit. A clear increase in O₃ loss-
301 rate constants can be observed when RH increases above 70-80% when a temperature inversion
302 was observed. A small increase at RH higher than 70-80% was also observed when temperature
303 inversions were absent. The observed dependence of $k_L(O_3)$ on relative humidity is consistent with
304 previous studies in forested regions, which have reported an increase in O₃ loss above 60-70% RH
305 (Altimir et al., 2006; Rannik et al., 2012; Zhou et al., 2017). Altimir et al. (2006) suggested an
306 enhancement factor which is humidity dependent above 70% RH; 1 at 70% RH, 2 at 85% RH and
307 a sharp increase to over 5 when moving towards 100% RH. In a boreal forest these observations
308 have been explained by the formation of a “wet skin” on leaves which enhances surface O₃ losses
309 by modifying (reducing) the surface-resistance to uptake (Zhou et al., 2017). This is in broad
310 agreement with our observations during nights with a temperature inversion (see Figure 4), and
311 the discrepancies between the studies could be explained e.g. by different tree types, the height of
312 the boundary layer, strength of the inversion and temperature.

313 The faster net rate of O₃ loss on nights with high relative humidity and well-defined temperature
314 inversions explain the differences observed in the O₃ mixing ratios at night during the Atlantic and
315 continental phases. The average nighttime (20:00-04:00 UTC) RH for the Atlantic phase was 87.4
316 ± 7.6 (1 σ) % compared to 68.4 ± 12.7 (1 σ) % for the continental phase, indicating that on nights
317 with temperature inversions higher loss-rate constants would be expected for the Atlantic phase.
318 The high RH combined with the significantly lower average peak O₃ mixing ratio in the Atlantic
319 phase (34.5 ± 6.0 (1 σ) ppbv between 14:00-15:00 UTC) compared to the continental phase (52.7
320 ± 13.6 (1 σ) ppbv between 14:00-15:00 UTC) explains why on nights with temperature inversions
321 during the Atlantic phase the O₃ was essentially completely depleted as shown in Figure 2 and S7.

322

323 4.2 Nitrogen Oxide Soil Emissions

324 Figure 2 (left panel) and S7 show nighttime periods in which NO was observed when O₃ was
325 depleted during the Atlantic phase. The several hours duration of the period when NO was above
326 the LOD excludes very local combustion as the source, leaving soil emissions resulting from
327 microbial activity (Davidson and Kinglerlee, 1997) as the most likely source of NO. At 293 K and
328 2 ppbv of O₃, the lifetime of NO towards reaction with O₃ is around 20 minutes. It is therefore
329 reasonable to assume that NO is close to steady-state when there is 2 ppbv or more of O₃ available.
330 The NO emission rate (E_{NO}) can therefore be equated to the loss rate of NO as described in equation
331 (1) assuming all peroxy radicals (XO₂) react with the same rate coefficient as HO₂:

$$332 E_{NO} = k_{NO+O_3}[NO][O_3] + k_{NO+HO_2}[XO_2][NO] \quad (1)$$

333 where k_{NO+O_3} and k_{NO+HO_2} are the temperature-dependent rate constants for the reaction between
334 NO and O₃ and HO₂, respectively, (IUPAC, 2024) and [NO], [O₃] and [XO₂] are the measured
335 concentrations of NO, O₃ and XO₂, respectively. In Figure 5, NO and E_{NO} (when O₃ > 2 ppbv) at
336 nighttime ($JNO_2 < 10^{-5} \text{ s}^{-1}$) are separated by air masses and plotted against O₃, where the outliers
337 are defined as being outside 1.5 \times interquartile range (IQR). While the nighttime NO mixing ratio
338 increased rapidly when O₃ tended towards 0 ppbv during the Atlantic phase, O₃ was never depleted
339 to less than 5 ppbv during the Continental phase and therefore no sustained periods of enhanced

340 NO were observed at nighttime. In contrast, no significant trend is found when plotting E_{NO} against
341 O_3 for either of the phases, which shows that the calculated soil emission of NO is not dependent
342 on O_3 . This indicates that while the soil is an important but variable source of NO, sustained
343 nighttime NO peaks are only observed above the instrument LOD when O_3 is almost totally
344 depleted so that the lifetime of NO is long enough to allow its concentration to build-up
345 sufficiently.

346 Water content and temperature have previously been shown to impact the emission rate of NO
347 from soil (Pilegaard, 2013; Rosenkranz et al., 2006). Rosenkranz et al. (2006) found a positive
348 correlation between soil moisture and NO emission up to 40% water-filled pore space (WFPS) and
349 an optimum between 12.5 and 15 °C soil temperature in a sessile oak forest in Hungary. In Figure
350 6, NO and E_{NO} are plotted against the soil temperature and moisture at 5 cm below the surface.
351 The measured NO mixing ratios peak towards the highest soil moisture and lowest soil temperature
352 measured during this campaign, however, as with O_3 , there is no significant trend in the NO
353 emission rates with soil moisture. At the low (11.5-12.5 °C) and high (19.5-20.5 °C) nighttime soil
354 temperatures very few measurements were made (around 2 hours combined) compared to the rest
355 of the temperature intervals. Across the remaining temperature intervals, no significant trend was
356 observed in the estimated NO emission.

357 The average NO emission rate derived for the two phases is identical with values of
358 1.45 ± 1.61 ppbv h^{-1} (1σ , median = 1.27 ppbv h^{-1}) and 1.42 ± 5.68 ppbv h^{-1} (1σ , median = 0.71
359 ppbv h^{-1}) for the Atlantic and Continental phases, respectively, when using data where $O_3 > 2$
360 ppbv. The Continental phase show much higher variability resulting from more spikes in the data
361 during that period. When O_3 is completely depleted during the Atlantic phase, the increase in NO
362 per hour results in NO emission rates of 0.3-1.8 ppbv h^{-1} , which is in reasonable agreement with
363 the averages across each of the two phases when there is still O_3 present. By assuming a mixed
364 nocturnal boundary layer (NBL) with a height of 20 m (top of the canopy), the average emission
365 rates can be converted to NO emission fluxes of 16.6 ± 18.5 (1σ) and 16.2 ± 65.0 (1σ) $\mu g N m^{-2} h^{-1}$,
366 respectively. These values are within the range of previous measurements in different European
367 forests with similar tree types to those found in the Rambouillet forest (see Table 1). The
368 measurements by Pilegaard et al. (2006) and Rosenkranz et al. (2006) were all performed using
369 the chamber technique, whereas Schindlbacher et al. (2004) measured the emission from soil
370 samples collected in the field and exposed to different temperatures and humidity in the laboratory.
371 The chamber-derived emission rates are all either lower or, within combined uncertainties, equal
372 to the values determined in this study, while emission rates from the soil samples were higher than
373 (or, within combined uncertainties, equal to) the values derived in the present study. Davidson and
374 Kinglerlee (1997) modelled the global NO emission inventory from soil depending on the biome
375 (e.g. temperate forest, agriculture, and savanna), and split the temperate forest category into
376 regions affected by nitrogen deposition or not. For temperate forests not affected by nitrogen
377 deposition, those authors estimated a flux of 0.0-0.2 $kg N ha^{-1} yr^{-1}$ (0.0-2.3 $\mu g N m^{-2} h^{-1}$), which is
378 in good agreement with the lower measurements by Pilegaard et al. (2006). In contrast, the
379 temperate forests impacted by nitrogen deposition had estimated fluxes of 1.1-5.0 $kg N ha^{-1} yr^{-1}$
380 (12.6-57.1 $\mu g N m^{-2} h^{-1}$), which is in good agreement with our measurements at Rambouillet where
381 nitrogen deposition is enhanced by pollution arriving from Paris and other surrounding urbanized

382 / industrialized areas. While noting that our fluxes are broadly consistent with previous
383 measurements, we recognise that the calculations are based on the assumptions of a well-mixed
384 boundary layer of fixed height arbitrarily set at 20 m and should not be over-interpreted.

385

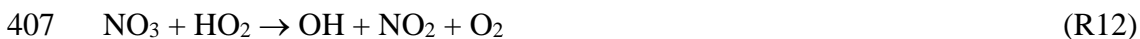
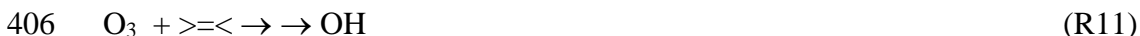
386 **4.3 Nitrogen Dioxide Losses**

387 At nighttime, in the absence of its photolysis, NO₂ may be expected to increase in concentration
388 (via R2) when a constant NO source exists (e.g. from soil, as observed here) and when O₃ is
389 present. For both the Atlantic and the Continental phases an average diel profile between 20.00
390 and 04.00 UTC of NO₂ (black) is plotted in Figure 7. No obvious increase in NO₂ can be observed
391 in the Atlantic phase and an average increase of around 1 ppbv can be observed in the Continental
392 phase. The expected NO₂ resulting from the NO + O₃ reaction if there were no loss mechanisms
393 of NO₂ is plotted in red. This is determined using the NO₂ measured at 20.00 UTC and
394 incrementing this value by the NO₂ that would have been produced through NO oxidation by O₃
395 and peroxy radicals in each time step. In both phases, the simple assumption of nighttime NO₂
396 production through NO + O₃ and NO + XO₂ and no NO₂ loss results in significant generation of
397 NO₂ with an overestimation of 10-12 ppbv of NO₂ at the end of the night compared to the measured
398 NO₂. A loss mechanism of around 1.4 ppbv h⁻¹ of NO₂ is therefore necessary to explain the
399 observed (lack of increase in) NO₂.

400

401 **4.3.1 Chemical Losses**

402 While during the daytime NO₂ is removed in a largely irreversible process through reaction with
403 OH radicals to form HNO₃, this is unlikely to represent a significant sink at nighttime. In the
404 absence of photochemical formation pathways, OH is generated at night in the ozonolysis of
405 olefins and in the reaction of HO₂ with NO₃ and NO.



409 In the forested environment in summer, the emissions of biogenic volatile organic compounds
410 (BVOC) (e.g. olefinic terpenoids) will favour R11 and simultaneously disfavour R12 as NO₃ will
411 be reduced in concentration through its reactions with BVOCs. During the ACROSS campaign
412 ground NO₃ levels were generally below instrument detection limits of 2 pptv and we can
413 reasonably ignore R12. Measurements of OH in forested environments are sparse, though they
414 indicate that nocturnal OH levels are low, with concentrations generally lower than 1 × 10⁵
415 molecule cm⁻³. Combining the rate coefficient for reaction of OH with NO₂ of ~1 × 10⁻¹¹ cm³
416 molecule⁻¹ s⁻¹ (IUPAC, 2024) at ambient pressure and ≈ 300 K with an upper limit (confirmed by
417 measurements) to the OH concentration of 1 × 10⁶ molecule cm⁻³ results in a NO₂ loss constant of
418 1 × 10⁻⁵ s⁻¹, or (at the average nighttime NO₂ = 1650 pptv) a loss rate of ~60 ppt h⁻¹, clearly
419 insufficient to explain the observations.

420 NO₂ is also lost via its reaction with O₃ to form the NO₃ radical (R8). In an upcoming paper, we
421 will show that the majority of NO₃ formed in the forest will react with BVOCs rather than with
422 NO (to re-form NO₂) and, to a good approximation, R8 represents an irreversible loss of NO₂ as
423 the alkyl nitrates will not release nitrogen in the form of NO₂ at nighttime. However, the rate
424 coefficient for this process ($3.5 \times 10^{-17} \text{ cm}^3 \text{ molecule}^{-1} \text{ s}^{-1}$ at 298 K, (IUPAC, 2024)) is very small
425 and with average nighttime O₃ levels reduced by deposition (see above) to 23 ppbv, the lifetime
426 of NO₂ with respect to this reaction is 14 hours and the loss-rate (at the average nighttime NO₂ =
427 1650 pptv) is $\sim 120 \text{ pptv h}^{-1}$, again too slow to contribute significantly to the apparent loss rate of
428 NO₂.

429 The chemical loss of NO₂ via reaction with OH or via formation of NO₃ and its further reactions
430 with BVOC to form alkyl nitrates is expected to result in the conversion of NO_X to NO_Y. As
431 described in section 3.1.1, during the ACROSS campaign we operated a NO_Y instrument to
432 measure NO_Y both in the gas- and particle-phases. Figure 8 displays the average diel profiles of
433 NO_Z (NO_Y-NO_X) and pNO₃ during the Atlantic and Continental phases. For both NO_Z and pNO₃
434 the diel profiles show either a decrease or stable mixing ratio across the period in which losses of
435 10-12 ppbv of NO₂ are required to explain the observations. Clearly, the loss of NO₂ at nighttime
436 is not balanced by the formation of other forms of reactive nitrogen that were long lived enough
437 to be detected. Trace gases such as HNO₃ or alkyl nitrates may be lost via deposition to surfaces,
438 especially at high relative humidity and lifetimes for biogenic alkyl nitrates of a few hours have
439 been reported (Liebmann et al., 2019; Farmer and Cohen, 2008; Browne et al., 2013; Romer
440 Present et al., 2019). However, as shown above, the limiting step in the formation of organic
441 nitrates is the slow reaction of NO₂ with O₃, which will not convert sufficient NO₂ to NO_Z to
442 explain our observations. Formation of organic nitrates that do not require the intermediacy of NO₃
443 (i.e. peroxy nitrates formed from RO₂ + NO₂) would also have been detected by the NO_Y
444 instrument and can thus also be ruled out as major reservoirs of NO_X.

445 NO₂ deposited to humid surfaces can be converted to HONO and released to the atmosphere
446 (Elshorbany et al., 2012; Meusel et al., 2016). A time series of HONO can be found in Figure S2
447 which reveals increases in HONO at nighttime. However, the HONO mixing ratios can account
448 for only a small fraction of the NO₂ loss described above. This may reflect the fact that, if formed
449 at a moist surface, (soluble) HONO is unlikely to desorb quantitatively into the gas-phase. The
450 low HONO mixing ratios measured during the Atlantic phase compared to the Continental phase,
451 could potentially be explained by the difference in soil humidity, however, the factors influencing
452 the formation and release of HONO are complex. The HONO observations will be analysed in
453 detail in a separate publication from the ACROSS campaign.

454 In the absence of other known gas-phase mechanisms for the removal of NO₂ at night and the fact
455 that very little other reactive nitrogen trace-gases or nitrate particles are formed during the night,
456 we conclude that physical removal of NO₂ (i.e. deposition) is responsible for its lack of build-up
457 at night during ACROSS and that any transformation of NO₂ at the surface does not lead to
458 quantitative release into the gas-phase

459

460 4.3.2 Physical Losses

461 NO₂ is known to be lost through dry deposition to surfaces such as soil and leaves, the latter
462 depending on whether the stomata are open (daytime) or not fully open (nighttime) (Delaria et al.,
463 2020; Delaria et al., 2018; Chaparro-Suarez et al., 2011). As for O₃, dry deposition of NO₂ to
464 surfaces can be described by an exponential decay with a first-order decay rate constant, $k_L(\text{NO}_2)$
465 = (V_d/h) , where V_d is the deposition velocity and h is the boundary layer height. This expression
466 applies when gradients within the boundary layer are weak, as expected for NO₂ (see above) even
467 though vertical mixing is very slow at night. The net production (or loss) of NO₂ is given by Eq.
468 (2) where the first term on the right-hand side is the NO₂ production rate from the reaction of NO
469 with O₃ or XO₂ (which is identical to the NO soil emission rate) and the second term is the loss
470 rate assuming only depositional losses (see above) and ignoring entrainment of NO₂ from other
471 heights. This will give an upper limit of the NO₂ deposition rate as a small fraction (<10%) of NO₂
472 is lost through chemical reactions with O₃ and OH (see above).

$$473 \frac{d[\text{NO}_2]}{dt} = E_{\text{NO}} - k_L(\text{NO}_2)[\text{NO}_2]_0 \quad (2)$$

474 [NO₂]₀ is the NO₂ mixing ratio at 20.00 UTC. The NO₂ concentration at any subsequent time can
475 then be calculated as described in Eq. (3) with variation of $k_L(\text{NO}_2)$ in order to match the observed
476 NO₂ mixing ratio.

$$477 [\text{NO}_2]_t = \int_0^t \frac{d[\text{NO}_2]}{dt} + [\text{NO}_2]_0 \quad (3)$$

478 In Figure 7 the grey lines symbolize the calculated NO₂ mixing ratios at nighttime using values of
479 $k_L(\text{NO}_2)$ between 1.0×10^{-4} and $4.0 \times 10^{-4} \text{ s}^{-1}$. As expected, no single value of $k_L(\text{NO}_2)$ can explain
480 all the measurements as the height of the BL will not be invariant during the whole night. However,
481 for the Continental and Atlantic phases the observed NO₂ can be explained with $k_L(\text{NO}_2) = (2.0 \pm$
482 $1.0) \times 10^{-4} \text{ s}^{-1}$ and $k_L(\text{NO}_2) = (2.75 \pm 1.25) \times 10^{-4} \text{ s}^{-1}$, respectively, which results in lifetimes of ~
483 1-3 h and ~ 40-110 min for NO₂ at nighttime. As deposition of NO₂ in this environment represents
484 a permanent loss of NO_x from the gas phase, this lifetime can be compared to e.g. the lifetime of
485 NO_x with respect to its conversion to HNO₃ via reaction of NO₂ with OH which is ~ 1 day
486 (assuming average [OH] = $1 \times 10^6 \text{ molecule cm}^{-3}$). The low aerosol surface area during ACROSS
487 combined with the low uptake coefficient for NO₂ renders losses due to heterogeneous processes
488 insignificant (IUPAC, 2024). Clearly, only nighttime-depositional losses of NO₂ in a forested
489 environment contribute substantially to its lifetime at night and to the NO_x budget.

490 If we continue to assume the nocturnal boundary layer at the forest site is at the top of the canopy
491 (20 m), then the NO₂ loss-rate constants we determined can be converted to a deposition velocity
492 of $0.4 \pm 0.2 \text{ cm s}^{-1}$ and $0.55 \pm 0.25 \text{ cm s}^{-1}$ for the Continental and Atlantic phase, respectively.
493 These are comparable to previous measurements of NO₂ deposition velocities of 0.15 cm s^{-1}
494 (Dewald et al., 2022), $0.1\text{-}0.57 \text{ cm s}^{-1}$ (Rondón et al., 1993), 0.098 cm s^{-1} (Breuninger et al., 2013),
495 $0.2\text{-}0.5 \text{ cm s}^{-1}$ (Horii et al., 2004), $0.02\text{-}0.64 \text{ cm s}^{-1}$ (Puxbaum and Gregori, 1998), for a mountain
496 observatory surrounded by coniferous trees, boreal coniferous forests, a temperate coniferous
497 forest, a temperate mixed deciduous forest, and a temperate oak forest, respectively, where a
498 combination of soil and foliage deposition is measured. Horii et al. (2004) saw an increase in

499 deposition velocity with increasing NO₂ mixing ratio; from 0.2 cm s⁻¹ at 1 ppbv to 0.5 cm s⁻¹ at 30
500 ppbv. Puxbaum and Gregori (1998) reported monthly averages of 0.02-0.64 cm s⁻¹, however, their
501 nighttime deposition velocities averaged below 0.05 cm s⁻¹. The deposition velocities determined
502 here are a factor of 5-40 higher than what has been measured for nighttime foliage deposition
503 velocities to the leaves of different trees native to California (Delaria et al., 2020; Delaria et al.,
504 2018), but in good agreement with measurements for daytime. It is, however, important to note
505 that the deposition velocities estimated here are upper limits as the estimation of the NO emission
506 rate is an upper limit and chemical loss of NO₂ is not taken into account. Using an average
507 nighttime NO₂ mixing ratio of 1650 and 1450 pptv for the Continental and Atlantic phase,
508 respectively, results in NO₂ deposition rates of $13.6 \pm 6.8 \mu\text{g N m}^{-2} \text{ h}^{-1}$ and $18.7 \pm 8.5 \mu\text{g N m}^{-2} \text{ h}^{-1}$,
509 which are in reasonable agreement with that measured for soil NO₂ deposition in a sessile oak
510 forest of $9.67 \pm 1.92 \mu\text{g N m}^{-2} \text{ h}^{-1}$ during the summer (Rosenkranz et al., 2006). The estimated NO
511 soil emission rate and NO₂ deposition rate are, within the uncertainties, identical, which means the
512 Rambouillet forest is not a significant direct source or sink of NO_x.

513

514 **5 Summary:**

515 Measurements of NO, NO₂, NO_y, and O₃ during the ACROSS campaign (June-July 2022) in the
516 Rambouillet forest southwest of Paris, France, have been used to gain insight into nighttime
517 processes controlling NO_x in an anthropogenically impacted forest environment. Based on
518 HYSPLIT back trajectories, two phases of the campaign were identified; one dominated by air
519 originating over the Atlantic Ocean (“Atlantic”), which on average had high relative humidity and
520 low O₃ mixing ratios, and one dominated by continental air masses from different
521 urban/industrialized regions (“Continental”), which on average had a lower relative humidity than
522 the Atlantic phase and higher O₃ mixing ratios. Strong diel profiles were observed in the O₃
523 measurements across the campaign with daytime peak mixing ratios varying from ~30 to 90 ppbv
524 and nighttime tending towards 0-10 ppbv. The daily variation was driven by a variable but
525 generally rapid O₃ deposition to soil and foliar surfaces, with a strong influence of relative
526 humidity (influencing the surface resistance to uptake) and inversion (influencing the rate of
527 entrainment of O₃ from above the canopy).

528 During the Atlantic phase, periods of sustained NO above the instrumental detection limit was
529 observed at nighttime when O₃ was sufficiently low (i.e. the NO lifetime sufficiently long). This
530 enabled the derivation of an average NO emission rate from the soil (E_{NO}) of $\sim 1.4 \text{ ppbv h}^{-1}$, which
531 was confirmed by the approximately linear increase in NO observed in the absence of O₃ in the
532 Atlantic phase. The estimated E_{NO} is in broad agreement with previous measurements in other
533 European temperate forests with tree types as found in the Rambouillet forest.

534 An increase in NO₂ at night would be expected when having a constant NO emission rate of
535 $\sim 1.4 \text{ ppbv h}^{-1}$ in the presence of O₃ as observed in this study, however, this was not the case. The
536 lack of increase in NO₂ was used to estimate first-order decay constants of $(2.0 \pm 1.0) \times 10^{-4} \text{ s}^{-1}$
537 and $(2.75 \pm 1.25) \times 10^{-4} \text{ s}^{-1}$ resulting in an effective lifetime of NO₂ of $\sim 0.5\text{-}3 \text{ h}$. The loss of NO₂
538 at nighttime is presumably driven by deposition to soil and foliar surfaces since the lifetime of
539 NO₂ towards its reactions with OH and O₃ at night is >28 and 14 h , respectively. By comparison,

540 the daytime lifetime of NO₂ with respect to loss by reaction with OH is about 1 day. We conclude
541 that the nighttime deposition of NO₂ is a major sink of boundary layer NO_x in this forested
542 environment.

543

544 **6 Data Availability:**

545 All data can be found on <https://across.aeris-data.fr/catalogue/>.

546

547 **7 Author contribution:**

548 All authors contributed with measurements. Data analysis was conducted by STA with
549 contributions from JNC and PD. CC and VM organized the field campaign with contributions from
550 the individual group leads. STA and JNC developed the manuscript with contributions from all
551 authors.

552

553 **8 Competing Interests:**

554 At least one of the (co-)authors is a member of the editorial board of Atmospheric Chemistry and
555 Physics

556

557 **9 Acknowledgements:**

558 STA is thankful to the Alexander von Humboldt foundation for funding her stay at MPIC.

559 PD gratefully acknowledges the Deutsche Forschungsgemeinschaft (project “MONOTONS”,
560 project number: 522970430).

561 The ACROSS project has received funding from the French National Research Agency (ANR)
562 under the investment program integrated into France 2030, with the reference ANR-17-MPGA-
563 0002, and it was supported by the French National program LEFE (Les Enveloppes Fluides et
564 l'Environnement) of the CNRS/INSU (Centre National de la Recherche Scientifique/Institut
565 National des Sciences de l'Univers). Data from the ACROSS campaign are hosted by the French
566 national center for Atmospheric data and services AERIS.

567 IMT Nord Europe acknowledges financial support from the CaPPA project, which is funded by
568 the French National Research Agency (ANR) through the PIA (Programme d'Investissement
569 d'Avenir) under contract ANR-11-LABX-0005-01, the Regional Council “Hauts-de-France” and
570 the European Regional Development Fund (ERDF).

571

572 **10 References:**

573 Altimir, N., et al.: Foliage surface ozone deposition: a role for surface moisture?, Biogeosciences,
574 3, 209-228, 10.5194/bg-3-209-2006, 2006.

575 Breuninger, C., et al.: Field investigations of nitrogen dioxide (NO₂) exchange
576 between plants and the atmosphere, *Atmos. Chem. Phys.*, 13, 773-790, 10.5194/acp-13-773-
577 2013, 2013.

578 Browne, E. C., et al.: Observations of total RONO₂ over the boreal forest: NO_x sinks and HNO₃
579 sources, *Atmospheric Chemistry and Physics*, 13, 4543-4562, 10.5194/acp-13-4543-2013,
580 2013.

581 Burkhardt, J. and Eiden, R.: Thin water films on coniferous needles: A new device for the study
582 of water vapour condensation and gaseous deposition to plant surfaces and particle samples,
583 *Atmospheric Environment*, 28, 2001-2011, [https://doi.org/10.1016/1352-2310\(94\)90469-3](https://doi.org/10.1016/1352-2310(94)90469-3),
584 1994.

585 Cantrell, C. and Michoud, V.: An Experiment to Study Atmospheric Oxidation Chemistry and
586 Physics of Mixed Anthropogenic–Biogenic Air Masses in the Greater Paris Area, *Bulletin of*
587 *the American Meteorological Society*, 103, 599-603, [https://doi.org/10.1175/BAMS-D-21-](https://doi.org/10.1175/BAMS-D-21-0115.1)
588 [0115.1](https://doi.org/10.1175/BAMS-D-21-0115.1), 2022.

589 Chaparro-Suarez, I. G., et al.: Nitrogen dioxide (NO₂) uptake by vegetation controlled by
590 atmospheric concentrations and plant stomatal aperture, *Atmospheric Environment*, 45, 5742-
591 5750, <https://doi.org/10.1016/j.atmosenv.2011.07.021>, 2011.

592 Cienciewicki, J. and Jaspers, I.: Air Pollution and Respiratory Viral Infection, *Inhalation*
593 *Toxicology*, 19, 1135-1146, 10.1080/08958370701665434, 2007.

594 Davidson, E. A. and Kinglerlee, W.: A global inventory of nitric oxide emissions from soils,
595 *Nutrient Cycling in Agroecosystems*, 48, 37-50, 10.1023/A:1009738715891, 1997.

596 Delaria, E. R. and Cohen, R. C.: A model-based analysis of foliar NO_x deposition, *Atmos. Chem.*
597 *Phys.*, 20, 2123-2141, 10.5194/acp-20-2123-2020, 2020.

598 Delaria, E. R., et al.: Laboratory measurements of stomatal NO₂ deposition to native California
599 trees and the role of forests in the NO_x cycle, *Atmos. Chem. Phys.*, 20, 14023-14041,
600 10.5194/acp-20-14023-2020, 2020.

601 Delaria, E. R., et al.: Measurements of NO and NO₂ exchange between the atmosphere and
602 *Quercus agrifolia*, *Atmos. Chem. Phys.*, 18, 14161-14173, 10.5194/acp-18-14161-2018, 2018.

603 Dewald, P., et al.: Fate of the nitrate radical at the summit of a semi-rural mountain site in Germany
604 assessed with direct reactivity measurements, *Atmos. Chem. Phys.*, 22, 7051-7069,
605 10.5194/acp-22-7051-2022, 2022.

606 Draxler, R. R. and Rolph, G. D.: HYSPLIT (HYbrid Single-Particle Lagrangian Integrated
607 Trajectory) Model access via NOAA ARL READY Website
608 (<http://ready.arl.noaa.gov/HYSPLIT.php>). NOAA Air Resources Laboratory, Silver Spring,
609 MD., 2011.

610 Elshorbany, Y. F., et al.: Impact of HONO on global atmospheric chemistry calculated with an
611 empirical parameterization in the EMAC model, *Atmos. Chem. Phys.*, 12, 9977-10000,
612 10.5194/acp-12-9977-2012, 2012.

613 Emberson, L. D., et al.: Ozone effects on crops and consideration in crop models, *European Journal*
614 *of Agronomy*, 100, 19-34, <https://doi.org/10.1016/j.eja.2018.06.002>, 2018.

615 Farmer, D. K. and Cohen, R. C.: Observations of HNO₃, ΣAN, ΣPN and NO₂ fluxes: evidence for
616 rapid HO_x chemistry within a pine forest canopy, *Atmos. Chem. Phys.*, 8, 3899-3917,
617 10.5194/acp-8-3899-2008, 2008.

618 Finkelstein, P. L., et al.: Ozone and sulfur dioxide dry deposition to forests: Observations and
619 model evaluation, *Journal of Geophysical Research: Atmospheres*, 105, 15365-15377,
620 <https://doi.org/10.1029/2000JD900185>, 2000.

621 Friedrich, N., et al.: Measurement of NO_x and NO_y with a thermal dissociation cavity ring-down
622 spectrometer (TD-CRDS): instrument characterisation and first deployment, *Atmos. Meas.*
623 *Tech.*, 13, 5739-5761, 10.5194/amt-13-5739-2020, 2020.

624 Ganzeveld, L. and Lelieveld, J.: Dry deposition parameterization in a chemistry general circulation
625 model and its influence on the distribution of reactive trace gases, *Journal of Geophysical*
626 *Research: Atmospheres*, 100, 20999-21012, <https://doi.org/10.1029/95JD02266>, 1995.

627 Gessler, A., et al.: NH₃ and NO₂ fluxes between beech trees and the atmosphere – correlation with
628 climatic and physiological parameters, *New Phytologist*, 147, 539-560,
629 <https://doi.org/10.1046/j.1469-8137.2000.00712.x>, 2000.

630 Geyer, A. and Stutz, J.: Vertical profiles of NO₃, N₂O₅, O₃, and NO_x in the nocturnal boundary
631 layer: 2. Model studies on the altitude dependence of composition and chemistry (vol 109, art
632 no D16399, 2004), *Journal of Geophysical Research-Atmospheres*, 109,
633 10.1029/2004JD005217 2004.

634 Hallquist, M., et al.: The formation, properties and impact of secondary organic aerosol: current
635 and emerging issues, *Atmospheric Chemistry and Physics*, 9, 5155-5236, 10.5194/acp-9-5155-
636 2009, 2009.

637 Heland, J., et al.: A new instrument to measure gaseous nitrous acid (HONO) in the atmosphere,
638 *Environmental Science & Technology*, 35, 3207-3212, DOI 10.1021/es000303t, 2001.

639 Hens, K., et al.: Observation and modelling of HO_x radicals in a boreal forest, *Atmospheric*
640 *Chemistry and Physics*, 14, 8723-8747, 10.5194/acp-14-8723-2014, 2014.

641 Horii, C. V., et al.: Fluxes of nitrogen oxides over a temperate deciduous forest, *Journal of*
642 *Geophysical Research: Atmospheres*, 109, <https://doi.org/10.1029/2003JD004326>, 2004.

643 IUPAC Task Group on Atmospheric Chemical Kinetic Data Evaluation, (Ammann, M., Cox, R.A.,
644 Crowley, J.N., Herrmann, H., Jenkin, M.E., McNeill, V.F., Mellouki, A., Rossi, M. J., Troe, J.
645 and Wallington, T. J.). Last access April. 2024: <https://iupac.aeris-data.fr/>, last
646 Jaeglé, L., et al.: Global partitioning of NO_x sources using satellite observations: Relative roles of
647 fossil fuel combustion, biomass burning and soil emissions, *Faraday Discussions*, 130, 407-423,
648 10.1039/B502128F, 2005.

649 Kanakidou, M., et al.: Organic aerosol and global climate modelling: a review, *Atmospheric*
650 *Chemistry and Physics*, 5, 1053-1123, 10.5194/acp-5-1053-2005, 2005.

651 Kane, S. M., et al.: Heterogeneous uptake of gaseous N₂O₅ by (NH₄)₂SO₄, NH₄HSO₄, and H₂SO₄
652 aerosols, *Journal of Physical Chemistry a*, 105, 6465-6470, 2001.

653 Kiendler-Scharr, A., et al.: Ubiquity of organic nitrates from nighttime chemistry in the European
654 submicron aerosol, *Geophysical Research Letters*, 43, 7735-7744, 10.1002/2016gl069239,
655 2016.

656 Kleffmann, J., et al.: Intercomparison of the DOAS and LOPAP techniques for the detection of
657 nitrous acid (HONO), *Atmospheric Environment*, 40, 3640-3652,
658 <https://doi.org/10.1016/j.atmosenv.2006.03.027>, 2006.

659 Kukui, A., et al.: Chemical ionisation mass spectrometer for measurements of OH and Peroxy
660 radical concentrations in moderately polluted atmospheres, *Journal of Atmospheric Chemistry*,
661 61, 133-154, 10.1007/s10874-009-9130-9, 2008.

662 Kurpius, M. R. and Goldstein, A. H.: Gas-phase chemistry dominates O₃ loss to a forest, implying
663 a source of aerosols and hydroxyl radicals to the atmosphere, *Geophysical Research Letters*, 30,
664 10.1029/2002gl016785, 2003.

665 Liebmann, J., et al.: Alkyl nitrates in the boreal forest: formation via the NO₃-, OH- and O₃-
666 induced oxidation of biogenic volatile organic compounds and ambient lifetimes, *Atmos. Chem.*
667 *Phys.*, 19, 10391-10403, 10.5194/acp-19-10391-2019, 2019.

668 Liebmann, J. M., et al.: Direct measurements of NO₃ reactivity in and above the boundary layer
669 of a mountaintop site: identification of reactive trace gases and comparison with OH reactivity,
670 *Atmospheric Chemistry and Physics*, 18, 12045-12059, 10.5194/acp-18-12045-2018, 2018.

671 Lightfoot, P. D., et al.: Organic peroxy radicals - kinetics, spectroscopy and tropospheric
672 chemistry, *Atmospheric Environment, Part A: General Topics*, 26, 1805-1961, 1992.

673 Meusel, H., et al.: Daytime formation of nitrous acid at a coastal remote site in Cyprus indicating
674 a common ground source of atmospheric HONO and NO, *Atmospheric Chemistry and Physics*,
675 16, 14475-14493, 10.5194/acp-16-14475-2016, 2016.

676 Padro, J.: Seasonal contrasts in modelled and observed dry deposition velocities of O₃, SO₂ and
677 NO₂ over three surfaces, *Atmospheric Environment. Part A. General Topics*, 27, 807-814,
678 [https://doi.org/10.1016/0960-1686\(93\)90002-G](https://doi.org/10.1016/0960-1686(93)90002-G), 1993.

679 Padro, J.: Summary of ozone dry deposition velocity measurements and model estimates over
680 vineyard, cotton, grass and deciduous forest in summer, *Atmospheric Environment*, 30, 2363-
681 2369, [https://doi.org/10.1016/1352-2310\(95\)00352-5](https://doi.org/10.1016/1352-2310(95)00352-5), 1996.

682 Phillips, G. J., et al.: The detection of nocturnal N₂O₅ as HNO₃ by alkali- and aqueous-denuder
683 techniques, *Atmospheric measurement techniques*, 6, 231-237, 10.5194/amt-6-231-2013, 2013.

684 Phillips, G. J., et al.: Significant concentrations of nitryl chloride observed in rural continental
685 Europe associated with the influence of sea salt chloride and anthropogenic emissions,
686 *Geophysical Research Letters*, 39, L10811, doi:10.1029/2012GL051912, 2012.

687 Pilegaard, K.: Processes regulating nitric oxide emissions from soils, *Philosophical Transactions*
688 *of the Royal Society B-Biological Sciences*, 368, ARTN 20130126
689 10.1098/rstb.2013.0126, 2013.

690 Pilegaard, K., et al.: Factors controlling regional differences in forest soil emission of nitrogen
691 oxides (NO and N₂O), *Biogeosciences*, 3, 651-661, 10.5194/bg-3-651-2006,
692 2006.

693 Puxbaum, H. and Gregori, M.: Seasonal and annual deposition rates of sulphur, nitrogen and
694 chloride species to an oak forest in north-eastern Austria (Wolkersdorf, 240 m a.s.l.), *Atmos.*
695 *Env.*, 32, 3557-3568, [https://doi.org/10.1016/S1352-2310\(98\)00073-9](https://doi.org/10.1016/S1352-2310(98)00073-9), 1998.

696 Rannik, Ü., et al.: Ozone deposition into a boreal forest over a decade of observations: evaluating
697 deposition partitioning and driving variables, *Atmos. Chem. Phys.*, 12, 12165-12182,
698 10.5194/acp-12-12165-2012, 2012.

699 Romer Present, P. S., et al.: The changing role of organic nitrates in the removal and transport of
700 NO_x, *Atmos. Chem. Phys. Discuss.*, 2019, 1-18, 10.5194/acp-2019-471, 2019.

701 Rondón, A., et al.: Dry deposition of nitrogen dioxide and ozone to coniferous forests, *Journal of*
702 *Geophysical Research: Atmospheres*, 98, 5159-5172, <https://doi.org/10.1029/92JD02335>,
703 1993.

704 Rosenkranz, P., et al.: Soil N and C trace gas fluxes and microbial soil N turnover in a sessile oak
705 (*Quercus petraea* (Matt.) Liebl.) forest in Hungary, *Plant and Soil*, 286, 301-322,
706 10.1007/s11104-006-9045-z, 2006.

707 Schindlbacher, A., et al.: Effects of soil moisture and temperature on NO, NO₂, and N₂O
708 emissions from European forest soils, *Journal of Geophysical Research: Atmospheres*, 109,
709 <https://doi.org/10.1029/2004JD004590>, 2004.

710 Schumann, U. and Huntrieser, H.: The global lightning-induced nitrogen oxides source, *Atmos.*
711 *Chem. Phys.*, 7, 3823-3907, 10.5194/acp-7-3823-2007, 2007.

712 Shepson, P. B., et al.: Determination of the relative ozone and PAN deposition velocities at night,
713 *Geophysical Research Letters*, 19, 1121-1124, 10.1029/92gl01118, 1992.

714 Sobanski, N., et al.: A five-channel cavity ring-down spectrometer for the detection of NO₂, NO₃,
715 N₂O₅, total peroxy nitrates and total alkyl nitrates, *Atmospheric Measurement Techniques*, 9,
716 5103-5118, 10.5194/amt-9-5103-2016, 2016.

717 Stutz, J., et al.: Vertical profiles of NO₃, N₂O₅, O₃, and NO_x in the nocturnal boundary layer: 1.
718 Observations during the Texas Air Quality Study 2000 *Journal of Geophysical Research-*
719 *Atmospheres*, 109, art. D12306, 10.1029/2003JD004209, 2004.

720 Thoene, B., et al.: Absorption of atmospheric NO₂ by spruce (*Picea abies*) trees, *New Phytologist*,
721 134, 257-266, <https://doi.org/10.1111/j.1469-8137.1996.tb04630.x>, 1996.

722 Val Martin, M., et al.: Large-scale impacts of anthropogenic pollution and boreal wildfires on the
723 nitrogen oxides over the central North Atlantic region, *Journal of Geophysical Research:*
724 *Atmospheres*, 113, <https://doi.org/10.1029/2007JD009689>, 2008.

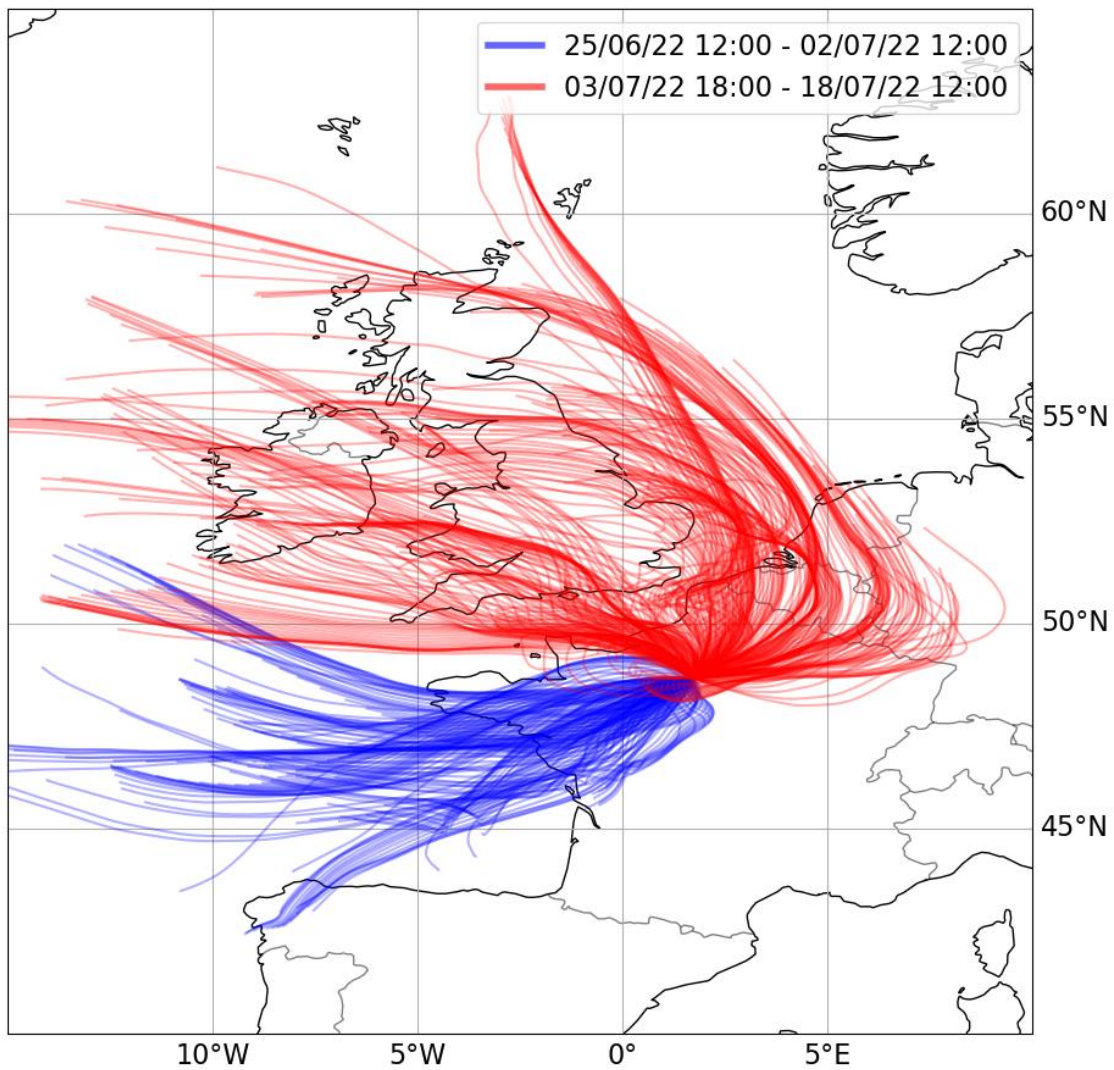
725 Weber, P. and Rennenberg, H.: Dependency of nitrogen dioxide (NO₂) fluxes to wheat (*Triticum*
726 *aestivum* L.) leaves from NO₂ concentration, light intensity, temperature and relative humidity
727 determined from controlled dynamic chamber experiments, *Atmospheric Environment*, 30,
728 3001-3009, [https://doi.org/10.1016/1352-2310\(96\)00008-8](https://doi.org/10.1016/1352-2310(96)00008-8), 1996.

729 Wu, Z., et al.: Dry deposition of O₃ and SO₂ estimated from gradient measurements above a
730 temperate mixed forest, *Environmental Pollution*, 210, 202-210,
731 <https://doi.org/10.1016/j.envpol.2015.11.052>, 2016.

732 Zhou, P., et al.: Simulating ozone dry deposition at a boreal forest with a multi-layer canopy
733 deposition model, *Atmos. Chem. Phys.*, 17, 1361-1379, 10.5194/acp-17-1361-2017, 2017.

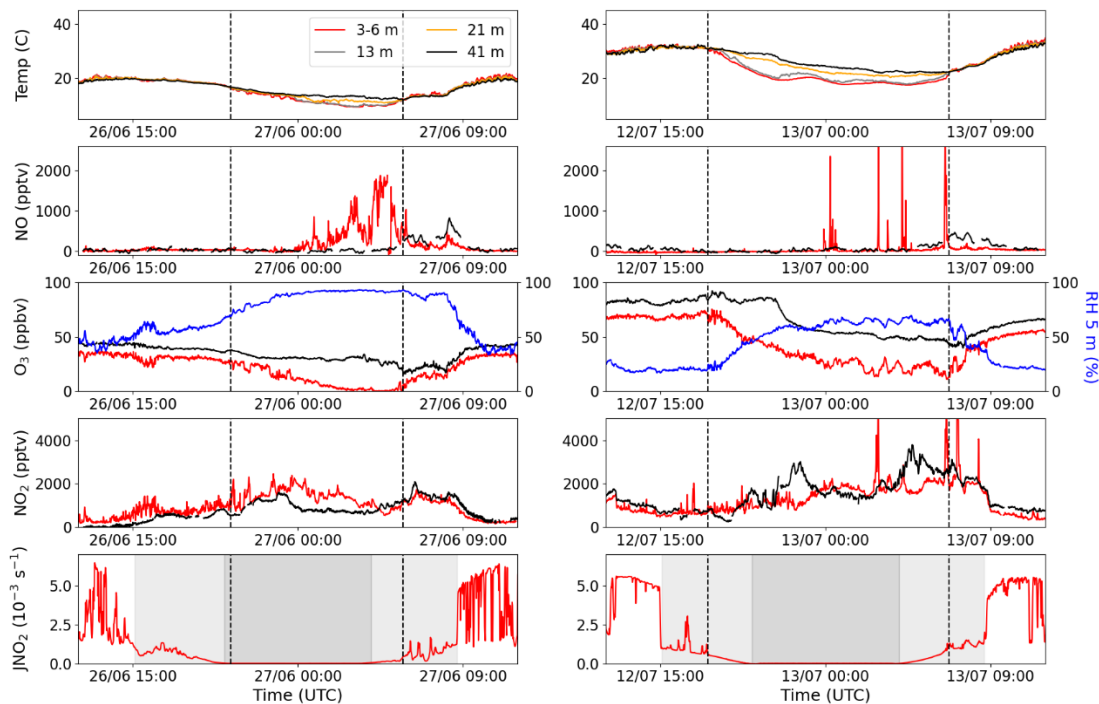
734

735 **11 Figures:**



736

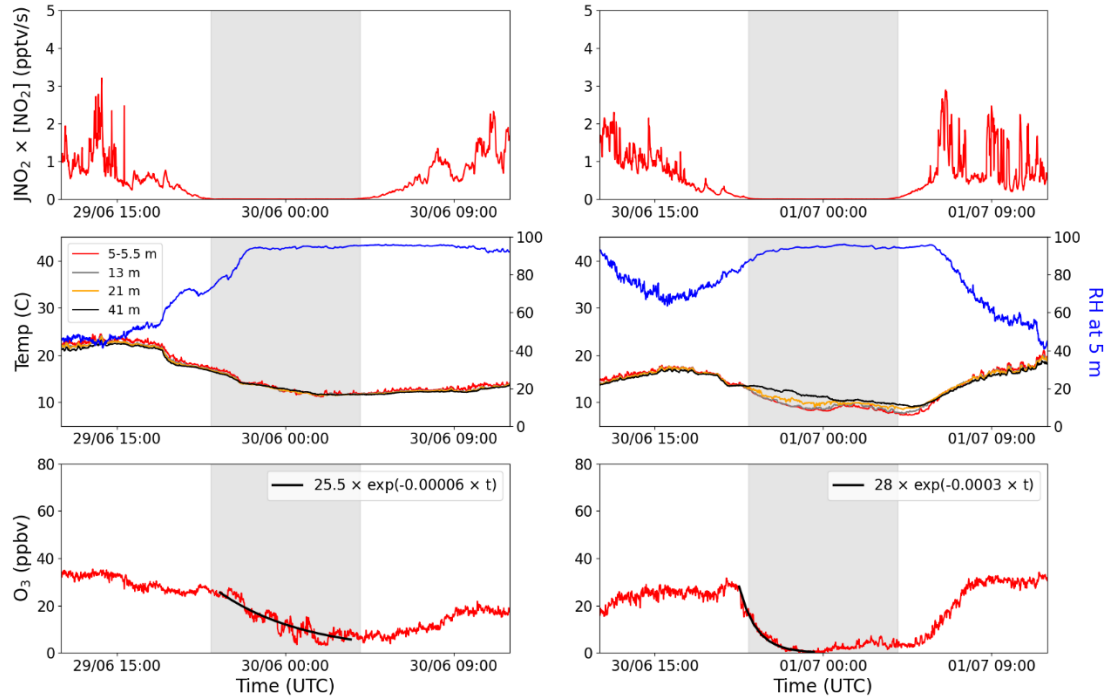
737 Figure 1: 48-hour back trajectories from the Rambouillet forest supersite using the Hybrid Single-
738 Particle Lagrangian Integrated Trajectory model (HYSPLIT, version 4, 2019).



739

740 Figure 2: Measurements of temperature, NO, O₃, RH, NO₂, and JNO₂ for two different nights
 741 during the campaign; one during the Atlantic phase (left panels) and one during the continental
 742 phase (right panels). The different colours symbolize four different heights; red = 3–6 m, grey =
 743 13 m, orange = 21 m, and black = 41 m, and the blue shows the RH at 5 m. The grey shaded areas
 744 in the JNO₂ plots shows the time the MPIC container was in shade during the afternoon and
 745 morning (light grey) and nighttime (dark grey). The vertical black dashed lines indicate the
 746 beginning and end of the observed temperature inversions in the top panels.

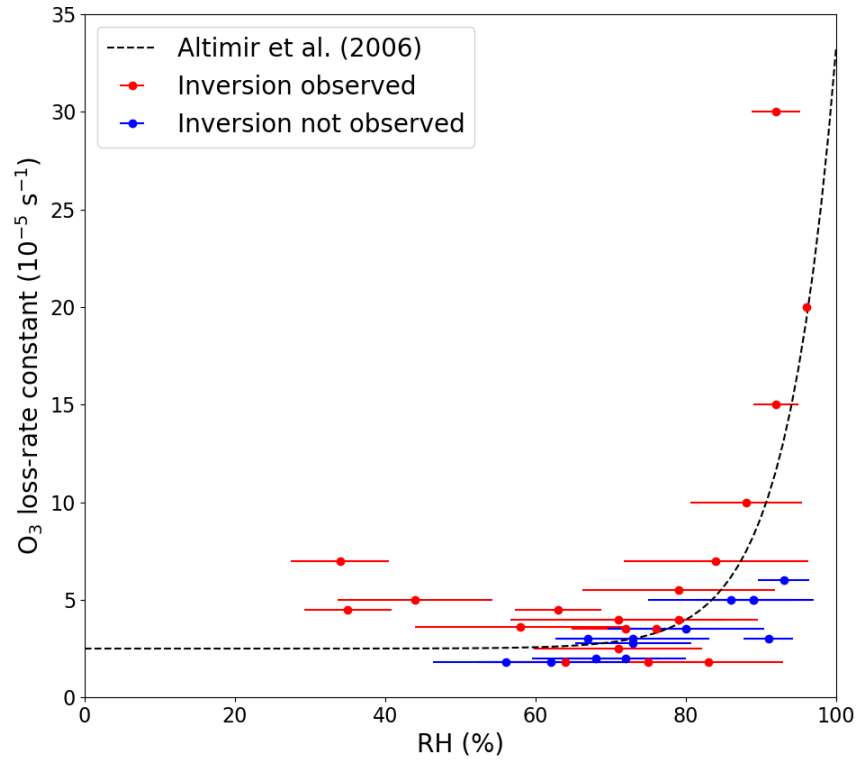
747



748

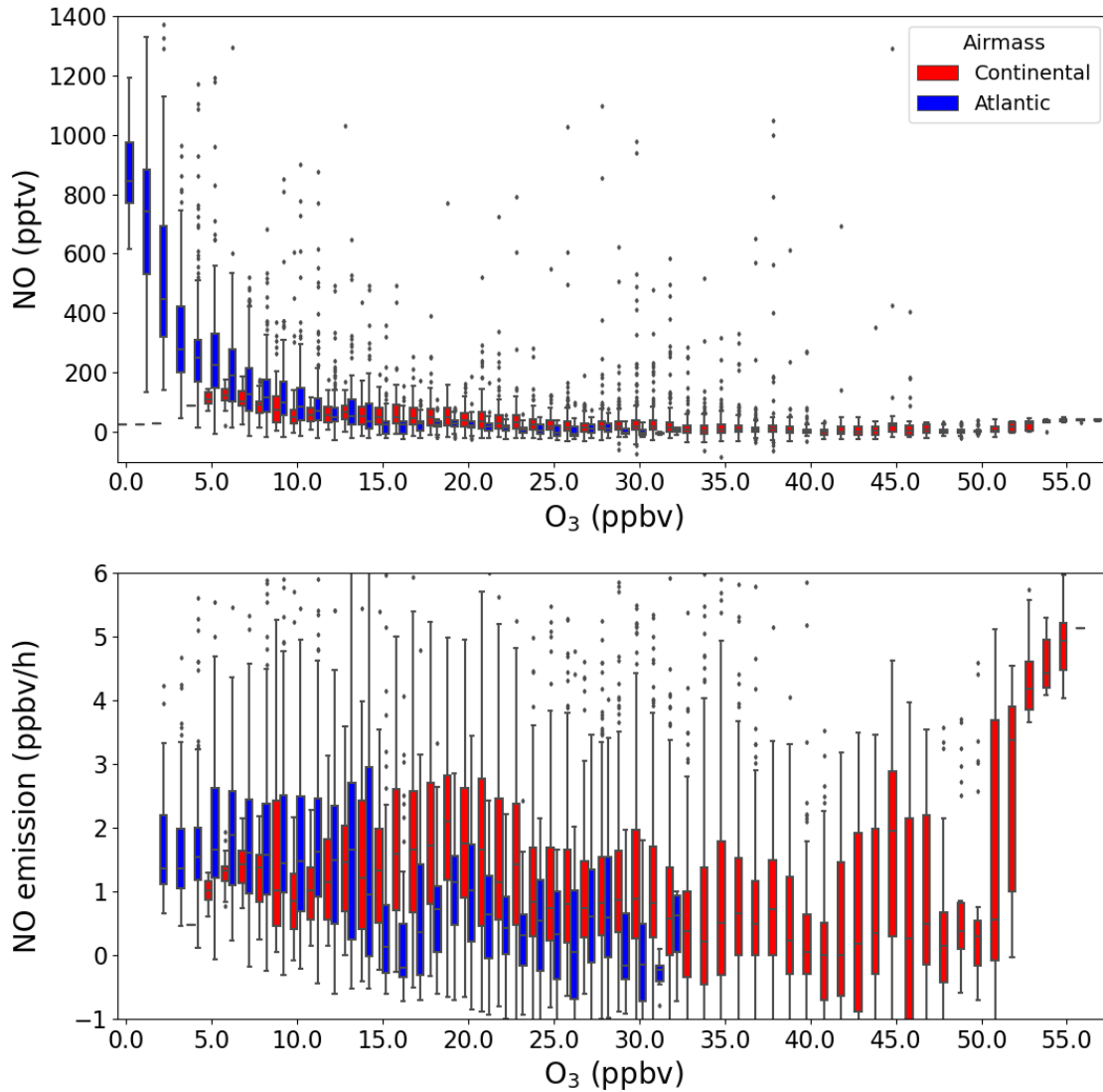
749 Figure 3: The production of O_3 ($JNO_2 \times [NO_2]$), temperature, RH, and O_3 plotted for two nights
 750 with high average RH; one without a temperature inversion (left panels) and one with a
 751 temperature inversion (right panels). The different colours symbolize four different heights; red =
 752 5-5.4 m, grey = 13 m, orange = 21 m, and black = 41 m, and the blue shows the RH at 5 m. The
 753 net nighttime O_3 loss is fitted with an exponential decay curve (solid black line) in the bottom
 754 plots. The grey shaded areas represent the nighttime.

755



756

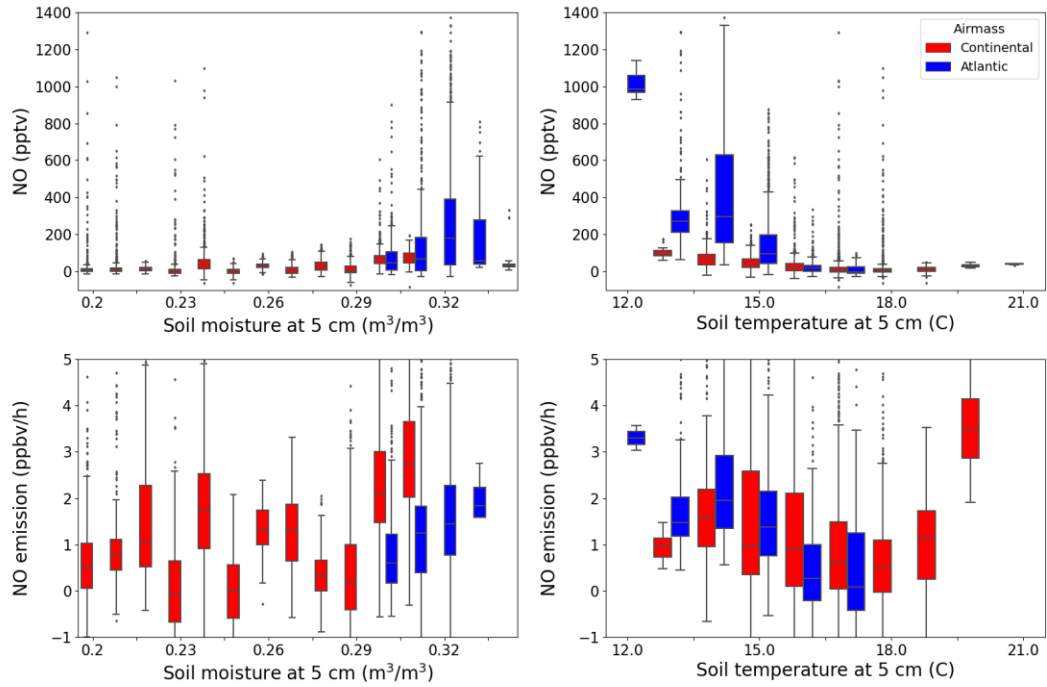
757 Figure 4: Net O₃ loss-rate constants at 5.4 m plotted against the average relative humidity measured
 758 during the time used to fit the exponential decay of O₃. The error bars represent ±1σ on the average
 759 RH. The dashed line symbolizes the observations made by Altimir et al. (2006).



760

761 Figure 5: NO (top) and NO emission (bottom) plotted against O₃ in a box-and-whiskers plot, where
 762 the outliers are defined as being outside $1.5 \times \text{IQR}$. The colours represent the two different air
 763 masses.

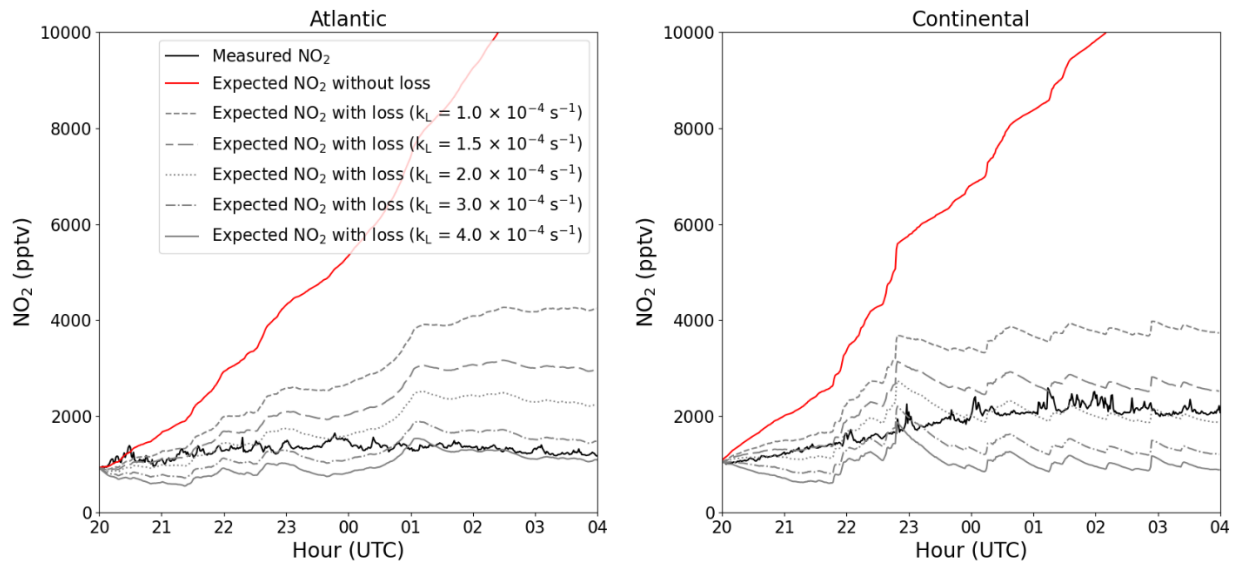
764



765

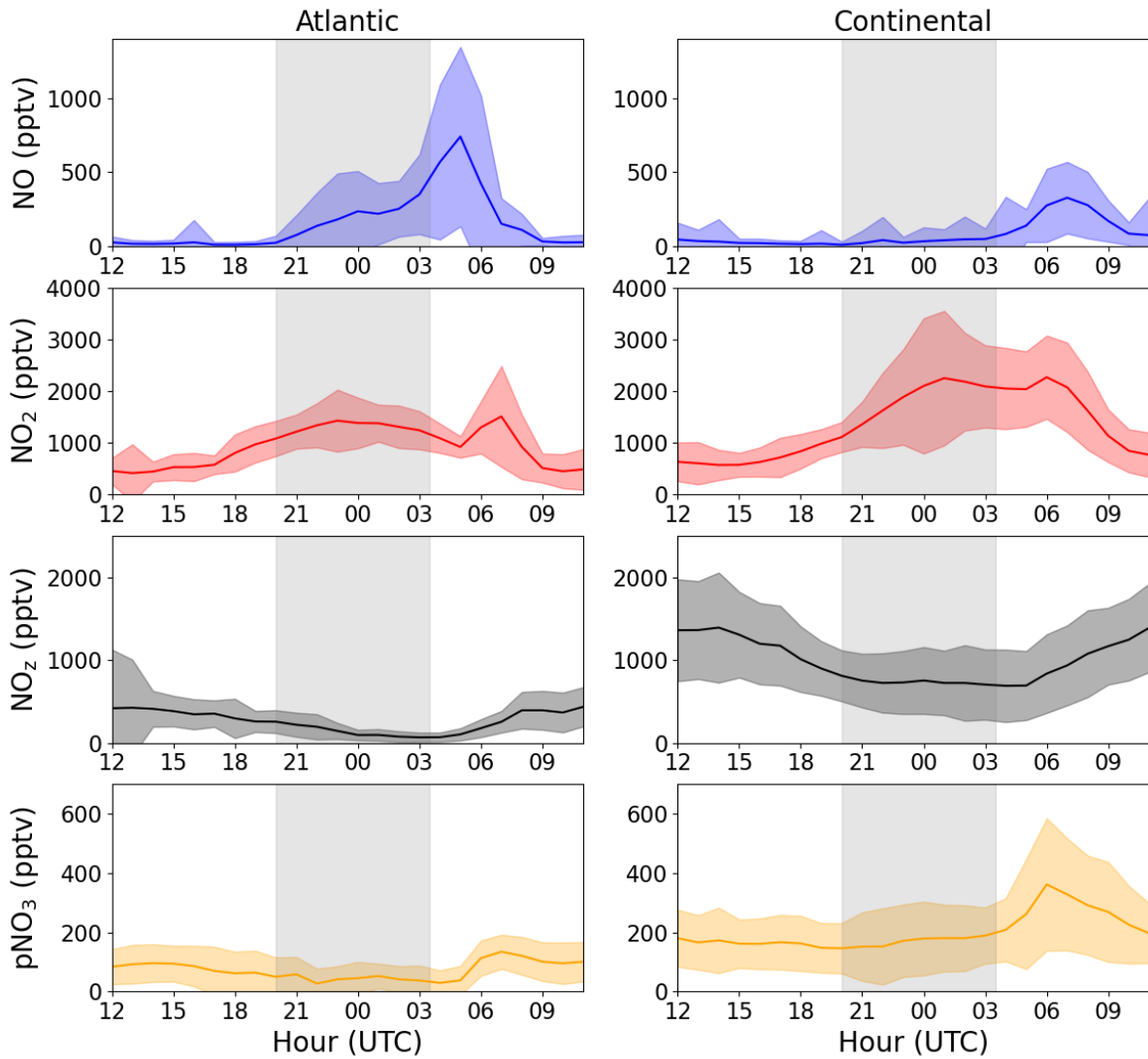
766 Figure 6: NO (top panels) and NO emission (bottom panels) plotted against soil moisture (left
 767 panels) and temperature (right panels) at 5 cm below the surface in a box-and-whiskers plot, where
 768 the outliers are defined as being outside $1.5 \times \text{IQR}$. The colours represent the two different air
 769 masses.

770



771

772 Figure 7: Average nighttime profiles of NO₂ at 5.4 m for each of the two phases (black) plotted
 773 together with the expected NO₂ with (grey) and without (red) NO₂ loss.



774

775 Figure 8: Average diel profiles of NO, NO₂, total gas-phase NO_z, and particulate nitrate (pNO₃) at
 776 3-6 m above ground for the Atlantic (left panels) and Continental (right panels) phases. The grey
 777 shaded areas symbolize nighttime.

778 **12 Tables:**

779

780 Table 1: Measured NO soil emission in European forests with the same tree types as in the
 781 Rambouillet forest.

Dominant tree type	Location	NO emission ($\mu\text{g N m}^{-2} \text{h}^{-1}$)	Reference
Oak	Matra Mountains, Hungary	2.1	(Pilegaard et al., 2006)
		6.0 ± 3.3 (summer)	(Rosenkranz et al., 2006)
		8.4 ± 2.4 (autumn)	(Rosenkranz et al., 2006)
Pine	San Rossore, Italy	5.4	(Pilegaard et al., 2006)
Beech	Schottenwald, Austria	25.5 ± 7.5	(Schindlbacher et al., 2004)
		4.2	(Pilegaard et al., 2006)
Beech	Klausen-Leopoldsdorf, Austria	10.2 ± 3.4	(Schindlbacher et al., 2004)
		0.7	(Pilegaard et al., 2006)
Spruce-Fir-Beech	Achenkirch, Austria	2.8 ± 1.4	(Schindlbacher et al., 2004)
		0.9	(Pilegaard et al., 2006)
Mixed deciduous	Ticino Park, Italy	18.5 ± 5.8	(Schindlbacher et al., 2004)
		Below LOD	(Pilegaard et al., 2006)

782

783